

Structure-function assessment of 3D-printed porous scaffolds by a low-cost/open source fused filament fabrication printer

Raúl Vallejos Baier ^{a,1}, José I. Contreras Raggio ^{a,1}, Carlos Toro Arancibia ^{a,1},
Miguel Bustamante ^{b,2}, Luis Pérez ^{c,3}, Iurii Burda ^d, Ameet Aiyangar ^{d,e,4}, Juan F. Vivanco ^{a,1,*}

^a Facultad de Ingeniería y Ciencias, Universidad Adolfo Ibáñez, Viña del Mar, Chile

^b Facultad de Ciencias Exactas, Universidad Andrés Bello, Santiago, Chile

^c Departamento de Ingeniería Mecánica, Universidad Técnica Federico Santa María, Valparaíso, Chile

^d Mechanical Systems Engineering, Empa - Swiss Federal Laboratories for Materials Science and Technology, Dübendorf, Switzerland

^e Department of Orthopaedic Surgery, University of Pittsburgh, USA



ARTICLE INFO

Keywords:

3D printer
Scaffold
Fused filament fabrication
Mechanical properties
Finite element method
Cell adhesion efficiency

ABSTRACT

Additive manufacturing encompasses a plethora of techniques to manufacture structures from a computational model. Among them, fused filament fabrication (FFF) relies on heating thermoplastics to their fusion point and extruding the material through a nozzle in a controlled pattern. FFF is a suitable technique for tissue engineering, given that allows the fabrication of 3D-scaffolds, which are utilized for tissue regeneration purposes. The objective of this study is to assess a low-cost/open-source 3D printer (In-House), by manufacturing both solid and porous samples with relevant microarchitecture in the physiological range (100–500 µm pore size), using an equivalent commercial counterpart for comparison. For this, compressive tests in solid and porous scaffolds manufactured in both printers were performed, comparing the results with finite element analysis (FEA) models. Additionally, a microarchitectural analysis was done in samples from both printers, comparing the measurements of both pore size and porosity to their corresponding computer-aided design (CAD) models. Moreover, a preliminary biological assessment was performed using scaffolds from our In-House printer, measuring cell adhesion efficiency. Finally, Fourier transform infrared spectroscopy – attenuated total reflectance (FTIR-ATR) was performed to evaluate chemical changes in the material (polylactic acid) after fabrication in each printer. The results show that the In-House printer achieved generally better mechanical behavior and resolution capacity than its commercial counterpart, by comparing with their FEA and CAD models, respectively. Moreover, a preliminary biological assessment indicates the feasibility of the In-House printer to be used in tissue engineering applications. The results also show the influence of pore geometry on mechanical properties of 3D-scaffolds and demonstrate that properties such as the apparent elastic modulus (E_{app}) can be controlled in 3D-printed scaffolds.

1. Introduction

A common solution in tissue engineering for bone regeneration is the creation of porous three-dimensional (3D) scaffolds, which once implanted into the defect site provide mechanical functions and facilitate the integration with the surrounding tissue [1,2]. The success of a

scaffold resides in some characteristics such as total porosity, pore size and interconnectivity, as well as mechanical and physicochemical properties [3–6]. Although it is accepted that pore size is an important variable affecting the ability of bone scaffolds to stimulate cell ingrowth and new bone formation [7,8], research on an optimal scaffold pore size for efficient bone regeneration remains inconclusive. For instance, some

* Corresponding author.

E-mail addresses: raul.vallejos@edu.uai.cl (R. Vallejos Baier), jcontrerasr@alumnos.uai.cl (J.I. Contreras Raggio), cartoro@alumnos.uai.cl (C. Toro Arancibia), m.bustamentespulveda@uandresbello.edu (M. Bustamante), luis.perez@usm.cl (L. Pérez), iurii.burda@empa.ch (I. Burda), ameet.aiyangar@empa.ch (A. Aiyangar), juan.vivanco@uai.cl (J.F. Vivanco).

¹ Address: Padre Hurtado 750, Viña del Mar, Chile. Zip code: 2520000.

² Address: República 239, Santiago, Chile. Zip code: 8320000.

³ Address: Avenida España 1680, Valparaíso, Chile. Zip Code: 2340000.

⁴ Address: Überlandstrasse 129, Dübendorf, Switzerland. Zip code: 8600.

early studies suggested that a minimum pore size of 100 µm enhances bone ingrowth [8–10], while other investigations have found that an optimal size is in the range of 100–500 µm [11]. The reason for uncertainty regarding optimal pore size may relate to variable interactions between the scaffold mechanical and physical properties, and the functional loading environment.

There are different approaches to manufacture tissue engineering scaffolds. One of these is 3D printing, which is an additive manufacturing technique that allows the fabrication of intricate structures from a computational model. Some of the main methods that encompass additive manufacturing are fused filament fabrication (FFF), inkjet printing, stereolithography and powder bed fusion [12]. FFF is based on heating thermoplastic filaments to their fusion point, in order to manufacture a structure in a layer-by-layer process. The method can theoretically achieve resolutions of the order of 100 µm, in terms of the minimum size of features, which allows the design and manufacture of bio-inspired scaffolds [13]. A promising emerging technology in additive manufacturing is also 3D bioprinting, which allows the use of biomaterials directly loaded with cells or other biological components (bioinks), making possible for better control regarding the biological interactions between the host and the printed structures [14]. Therefore, these technologies have applications in medical fields such as orthopedics, by means of repairing tissues with low or no capacity for self-repair, like articular cartilage and menisci [15].

Bone tissue can also present limitations for its self-healing capacities, as in critical-sized defects, in which bone grafts can become necessary [16]. The limitations in the access to natural bone grafts may open the possibilities for additive manufacturing approaches to offer new cost-effective solutions. Nevertheless, although the field is rapidly developing its potential for clinical practice and other applications, several limitations and pitfalls are still encountered, such as the variability, scalability and repeatability during the process [17]. These limitations require more studies that both characterize and standardize different aspects of the additive manufacturing process.

A challenge in additive manufacturing is to control the desired printing parameters, given that these can affect the mechanical [18] and geometrical [19] features of the manufactured structures. For example, parameters like infill pattern and density (the organization and proportion of solid material inside a structure), which can optimize 3D printing time, can affect the tensile strength of the manufactured samples [20]. More generally, polymer specimens and composites used in additive manufacturing procedures such as FFF can show diverse mechanical responses in terms of tensile, compression, flexural or impact strength by varying process parameters [18,21–23].

Even if a set of process parameters are selected for a desired design, the consistency and repeatability of the manufactured structures is variable and needs to be quantified. This becomes relevant for biomedical applications [24], given that cells within a biological context will sense their environment in a 3D-printed porous structure (scaffold) at the microscopic pore level [25].

After quantifying the variability of the manufactured scaffolds in terms of parameters like their mechanical responses, finite element analysis (FEA) becomes a powerful tool to compare these responses with an ideal theoretical model. FEA is a common numerical method that has been used to simulate mechanical properties of 3D scaffolds [26–28], as well as the distribution of surface strains [29] and the influence of different repeating unit cells on their mechanical behavior [30], among other applications.

The need for rapid prototyping approaches to manufacture tissue scaffolds for clinical applications comprises different stages, such as design, fabrication, and assessment. Each of these stages requires several considerations and possesses challenges, and need to work in a loop within a platform that constantly goes back to the design stage for scaffold optimization [31]. Correspondingly, the emergence of open source and low-cost devices, which overcomes the costs and limitations of commercially available technology, can be an attractive approach

within this platform for both science and engineering [32]. 3D-printing by commercially available low-cost FFF printers is an approach not only to fabricate scaffolds to evaluate their material properties and dimensional accuracy [33], but also to use them as models for tissue engineering applications [34]. Hence, open source FFF printing has also emerged as a cost-efficient approach in tissue engineering, allowing the fabrication of scaffolds made of a variety of materials [35].

The use of controlled models by FFF also allows for the implementation of *in vitro* experiments to evaluate biological responses to variables like bioactive coatings in scaffolds [36], or the influence of geometry and different materials [37]. Among the variety of polymers that can be used in FFF, polylactic acid (PLA) emerges as a suitable candidate, which is an aliphatic polyester produced from renewable sources [38]. Remarkably, PLA is not only biodegradable and biocompatible [39], but also is considered a low-cost material for 3D-printing [40], becoming one of the most studied polymers used in a variety of applications, among them, biomedical applications [38,41–44].

PLA can also be used as filaments of either pure polymer, or composites with a wide variety of materials such as nanohydroxyapatite [45], tricalcium phosphate [46], calcium carbonate [47], graphene oxide [48] and boron nitride [49], among others. Comprehensively, this biomaterial allows the manufacture of scaffolds to be used in additive manufacturing and tissue engineering [50–52]. Hence, PLA is an attractive polymer to be used for bone [2,53] and orthopedic applications [54]. In this regard, it is also noteworthy that PLA is a FDA-approved polymer [55,56].

The objective of this study is to assess the structure-function relationship during the manufacture of tissue engineering scaffolds with physiological microarchitecture, by a low-cost/open-source FFF printer.

2. Materials and methods

Porous samples were manufactured in our printer and were compared with samples manufactured in an equivalent commercial desktop FFF printer, in terms of microstructure and compressive mechanical performance. To assess the mechanical isotropy of solid samples, cubes were manufactured in both printers and assayed in three different orientations. To analyze the resolution limits in our printer, an infill analysis was performed. Additionally, for the compressive testing of porous samples, FEA models were used, to compare the responses with an expected theoretical value. Additionally, to assess the feasibility of our printer to be used in tissue engineering applications, a preliminary biological assessment was performed for cell adhesion efficiency. Finally, to explore if chemical changes in the PLA occur after 3D printing, Fourier transform infrared spectroscopy – attenuated total reflectance (FTIR–ATR) was performed to analyze the filament both before and after extrusion in each printer.

2.1. 3D-printers

A Grid II+ Desktop 3D Printer (Makerbot, USA) (hereafter called “Commercial printer”), and a custom-made 3D-Printer (hereafter called “In-House printer”) were used to fabricate porous scaffolds. The In-House 3D-printer uses the free access software “Repetier Host” for the printing parameters for each CAD model. Like a commercial printer, some parameters that can be modified are the fill percentage, number of shells, extrusion temperature and extrusion speed. The software also allows changing other more advanced parameters, such as printing speed for the supports, the height of the first layer, defining fill patterns, among others. Once the model file is imported in STL format, it creates a preview of the object to be printed, with the trails for each layer and the estimated printing time.

The In-House printer is controlled by an electronic board (Arduino, <https://www.arduino.cc/>), making it possible to reprogram it. On the other hand, the printer has two heads, which are programmed to maintain a minimum separation of 20 mm, avoiding possible collisions

with each other. These heads move with respect to the horizontal axes, while the base performs the movements in the vertical axis. Before starting each print, the printer automatically calibrates using touch sensors on each axis to define the printing space in which it will work (with the particularity of having a double sensor on the vertical axis at each end to level the base). The maximum printing space corresponds to $200 \times 200 \times 200$ mm.

Regarding its electronic components, the In-House 3D-printer counts with a control board MKS 1.4GEN, based on ATMEGA 2560. A motor controller A4988, a step motor Nema17 (CASUN) of 5 kg/cm and torque for XYZ axes, and another step motor Nema17 (CASUN) with reducer 15 kg/cm and torque for the extruders. Heads Bowden V5, a thermistor NTC100, a ceramic heater 40 W/12 V, a heat bed of 200×200 mm, Bluetooth and USB connection, and a switching source of 12 V/29A.

Regarding its mechanical components, the In-House 3D-printer counts with a linear bearing LM08, steel bars of 8 mm, pulleys GT2 16 T and belt GT2. Lastly, the equipment is within an aluminium composite structure.

2.2. 3D printing settings and material

The settings used for fabrication of all samples in both 3D printers were 100% infill, 215 °C extrusion temperature, 0.15 mm layer height, 60 mm/s feed rate and one layer of external shell, using a 0.4 mm nozzle. Commercial PLA filaments of 1.75 mm diameter (Verbatim, Charlotte, USA) were used for all scaffolds.

2.3. Sample design

2.3.1. Solid samples

All CAD models in this study were designed in Inventor Autodesk Professional (version 2021). To compare the isotropy of the material for compression tests, solid cubes of $5 \times 5 \times 5$ mm were manufactured, which were then tested in three different orientations.

2.3.2. Porous samples

To assess the microarchitecture in terms of pore size and porosity, compressive behavior, and preliminary biological performance in terms of cell adhesion efficiency, porous scaffolds of porosity close to 50% and strut thickness and pore size of 300 µm (Design 1) and 500 µm (Design 2) were manufactured following a continuous orthogonal lattice, with external dimensions of 5 mm (width) \times 5 mm (length) \times 4.807 mm (height).

To compare the microarchitecture resolution fidelity, a CAD model was designed which consisted in struts of variable spacing with external dimensions $21 \times 21.02 \times 3$ mm, allowing for the creation of 81 pores which ranged in areas from 0.81 mm^2 to 0.01 mm^2 (see Supplementary materials).

To assess the resolution fidelity of the In-House printer by an infill analysis, a cube of $15 \times 15 \times 15$ mm was manufactured with variation in its infill from 10 to 90%.

2.4. Microarchitectural characterization

The samples were photographed using a binocular stereoscope (Leica, Germany). To measure pore size and area, ImageJ software (version 1.8.0_112, NIH) was used for a representative sample with the ROI manager command [57,58]: A line or rectangle was drawn in each pore of the calibrated images, in order to measure their diameter or area, respectively. Similar methodologies for image dimension measurements have been used elsewhere [59]. The values of each pore area were converted to their corresponding circular equivalent diameter [60] by using the formula: Equivalent diameter = $(4A/\pi)^{1/2}$, in which "A" is the area of each measured square pore. All measurements of pore size are based in this transformation (unless indicated).

The experimental porosity was determined based on the liquid

displacement method with ethanol (95%, Winkler, CAS number 64–17–5) ($\rho = 0.81 \text{ g/ml}$ at 15–16 °C) [61] ($N = 6$), using an analytical scale with a density determination kit (Radwag, Poland) and the formula:

$$\text{Porosity} = 1 - \left(\frac{\text{Volume of displaced ethanol}}{\text{Total volume of the sample}} \right) \quad (1)$$

2.4.1. Optical microscopy

Optical microscopy (Zeiss Stemi SV11, Germany) was performed on representative samples for each of the four groups (In-house printer designs 1 and 2; commercial printer designs 1 and 2) to evaluate the 2-D cross-sectional dimensions of the printed struts and the accompanying pores. The goal was to verify that the porosity is maintained internally in the samples and not just restricted to the surfaces.

2.5. Mechanical characterization

To evaluate the mechanical behavior in solid cubes (infill 100%) in three different orientations (Figs. 1 and 2), and in scaffolds of both designs, uniaxial loading compressive testing was performed following the standard ASTM D695, using a universal electro-mechanical testing machine (Test Resources, USA) at a displacement rate of 1.3 mm/min with an 8-kN load cell.

The apparent elastic modulus (E_{app}) of the porous samples (or elastic modulus in the solid samples) was obtained from the slope of the linear segment of the strain-stress curves. For this, the stiffness of the bulk samples was converted using Hooke's law of elasticity in elastic solids by following the formula $E_{app} = KL/A$, in which "A" is the specimen cross-sectional area and "L" is the length parallel to loading direction.

The yield stress, defined as the stress at which the stress-strain curve becomes markedly nonlinear, was measured in solid samples following the indications for polymers [62]. Whenever this transition was not apparent, the intersection between the strain-strain curve and a 1% offset of the strain value was defined as the yield stress [63].

2.6. Numerical simulation

To evaluate the E_{app} during compression tests of the theoretical porous models, a commercial FEA package (ANSYS v19.1) was used. An equivalent compressive z-axis displacement (u_z) of 1% of the specimen's height was applied on the upper end of the studied cubes. Nodes of 10-node tetrahedral structural solid elements were employed for meshing. The number of nodes ranged from 3.2 to 3.6×10^5 , while the number of elements ranged from 7.8 to 8.8×10^4 .

To ensure appropriate numerical approximation, mesh convergence analysis was carried out by gradually increasing the number of elements and verifying the local stress behavior.

The coupled-node boundary condition (BC) (keeping selected nodes in the same plane) was used for the upper face of the modeled cubes. This condition is applied since the presence of pores results in un-even surfaces and therefore some problems on the numerical FEA displacement field could arise. On the other hand, BC in the bottom end of modeled cubes was set in $u_z = 0$.

The E_{app} used for FEA simulations was obtained from the compressive test of solid cubes of $5 \times 5 \times 5$ mm. described in Section 2.3.1, this parameter is called E_0 .

Using the numerical approximation provided for the FEA technique, the E_{app} of each scaffold models can be estimated from the response of the simulated compression test, and along the z-axis E_z^{FEA} by:

$$E_z^{FEA} = \frac{\sigma_z}{\varepsilon_z}, \quad (2)$$

where σ_z and ε_z are the stress and strain in z-axis, respectively. The applied displacement u_z (1% of the specimen's height) is used for determining the strain ε_z presented in Eq. (2).

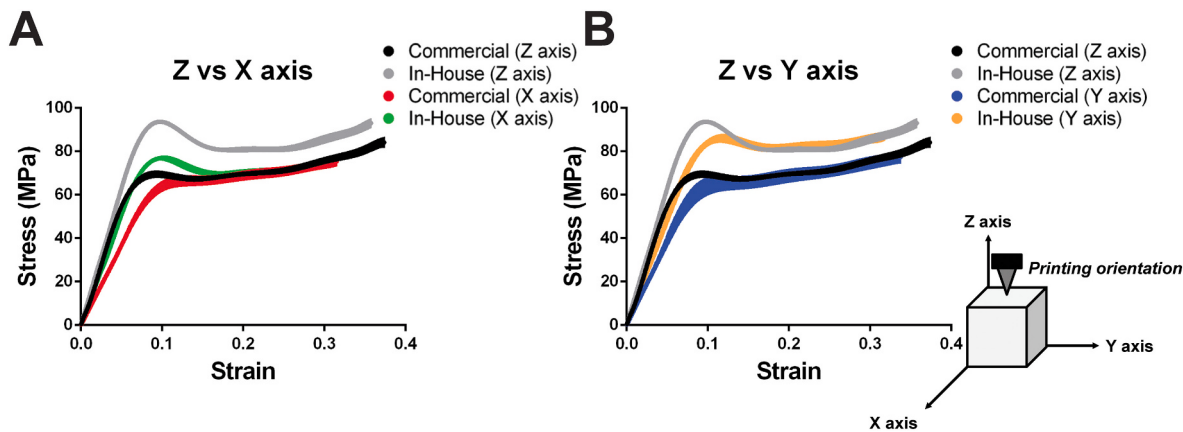


Fig. 1. Strain-Stress curves of solid cubes manufactured in both FFF printers. (A) Strain-stress curve comparing the Z and X axis during the compression of solid cubes manufactured in both printers. (B) Strain-stress curve comparing the Z and X axis during the compression of solid cubes manufactured in both printers (see inset for axis details), the width of each curve represents the SD with the mean as the middle line.

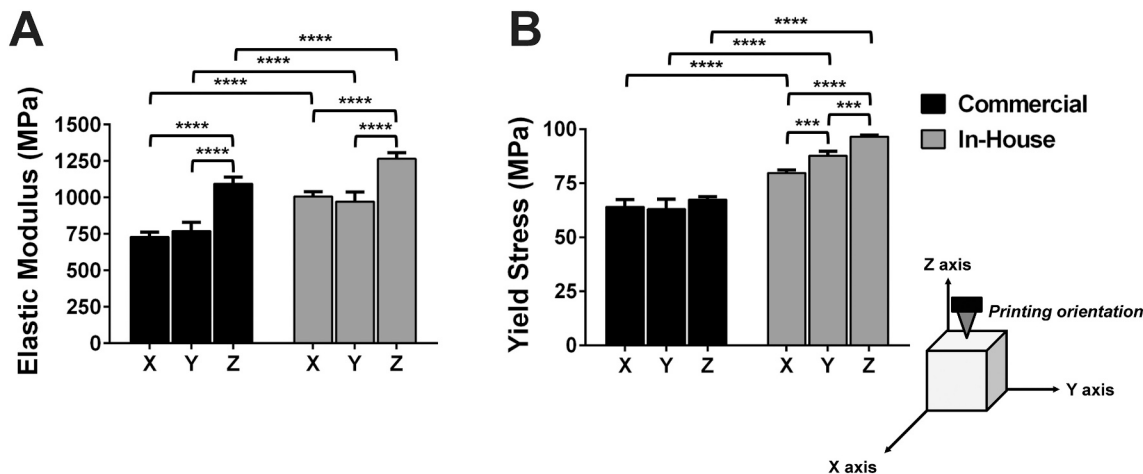


Fig. 2. Solid cubes manufactured in both FFF printers are transversally isotropic in their E_{app} in the X-Y axes. (A) The bar graph shows the elastic modulus for the solid cubes manufactured in both FFF printers tested in all three different orientations. (B) The bar graph shows the yield stress for the solid cubes manufactured in both FFF printers tested in all three different orientations (see inset for axis details). Columns represent the mean with the SD. In all cases, The Z axis represents the default printing plane. Brackets represent statistical significance in a post-hoc Tukey test after ANOVA (* = $p < 0.05$, ** = $p < 0.01$, *** = $p < 0.001$, **** = $p < 0.0001$).

$$\epsilon_z = \frac{u_z}{L_z}, \quad (3)$$

where L_z is the original height of the cubic specimen. The stress σ_z necessary for solving Eq. (2) is obtained using the following equation:

$$\sigma_z = \frac{F_z}{A_z}, \quad (4)$$

being F_z the reaction force in z-axis supported for the nodes located in the bottom end of modeled cubes, while A_z is the nominal area of this surface.

2.7. Biological characterization

To evaluate the feasibility of biological performance assessment in the In-House printer, a cell adhesion efficiency test was carried out. For this, a heterogenic population of human gingival mesenchymal stem cells (hGMSCs) were used [64,65], which were acquired from a small biopsy (5 mm) of the gingiva of 30–40 years old participants under local anesthesia (see [66]). A written informed consent from each volunteer was obtained, together with the approval by the Institutional Review Board of the University (see [66]). The protocol for cell isolation and maintenance was based on published methods [66–68].

PLA scaffolds manufactured in the In-House FFF printer (Designs 1 and 2) were treated with NaOH 0.1 M at 65 °C for 45 min to improve cell adhesion [36,69], rinsed twice with distilled water and then sterilized by ethanol 70% overnight. The next day, scaffolds were rinsed twice with sterile PBS 1× and left for 1 h in supplemented DMEM. For cell seeding, agarose molds were used for each scaffold (based on [36], see supplementary materials), using 2% agarose in PBS 1× (sterilized with UV light for 30 min). When reaching approximately 90–100% confluence, hGMSCs of passage 8 were trypsinized for scaffold seeding. Cell counting/viability were measured with an automated cell counter Luna-II (Logos Biosystems, South Korea).

To test cell adhesion efficiency, 1×10^5 cells in 50 µl of supplemented DMEM were used to seed each scaffold inside the mold ($n = 3$) in a 24-well tissue culture plate, using scaffolds seeded with 50 µl of supplemented DMEM without cells as blank controls for noise signal subtraction, together with 1×10^5 cells seeded on tissue culture plates or supplemented DMEM without cells added to tissue culture plates as positive and negative controls, respectively. After 3 h at 37 °C to allow for cell adhesion, tissue culture plates were filled with supplemented DMEM and kept at standard conditions until the next day, when all wells were rinsed three times with sterile PBS 1× to remove non-adherent cells [70]. Then, the scaffolds were transferred without their molds to a new tissue culture plate coated with agarose to prevent cell adhesion to

the plastic (a layer of 2% agarose in PBS 1×, previously sterilized by UV light for 30 min), with 1 ml of supplemented DMEM. After all scaffolds were transferred, 200 μ l of the reagent CellTiter 96® AQueous One Solution Cell Proliferation Assay (MTS, Promega) was added to each well (and the controls). After 2 h at 37 °C to develop the reaction, 200 μ l of each supernatant was homogenized by pipetting and transferred to a 96-well plate to measure the optical density (OD) at 490 nm in a plate reader (Bioteck 800 TS, USA). Cell adhesion efficiency is expressed in relation to the control (cells in well). Similar methodologies have been used elsewhere [51].

2.8. Fourier transform infrared spectroscopy – attenuated total reflectance (FTIR-ATR)

The ATR-FTIR measurements of the polymers before and after FFF in both 3D-printers were performed with a Cary 640 FTIR spectrometer (Agilent). A diamond ATR accessory with a type IIa synthetic diamond crystal has a penetration depth of ~2 μ m. The spectra were recorded in a frequency range of 4000–600 cm^{-1} with a spectral resolution of 4 cm^{-1} . A total of 64 scans were co-added for every spectrum. The background was measured with the same settings against air. The spectrometer was controlled by Agilent Resolutions Pro software 5.2.0.

2.9. Statistical analyses

All results were expressed as means with standard deviations (SD). To investigate the effects of the manufacture in both printers in the

elastic modulus of solid cubes ($N = 5$) and E_{app} of scaffolds ($N = 5$ por In-House samples, $N = 4$ for Commercial samples), a one-way ANOVA and Tukey's Honestly Significant Difference (HSD) *post hoc* test were performed using R (version 4.0.2). Using the same methodology for the biological assessment ($N = 3$). In all cases, the significance level was set at $\alpha = 0.05$. Additionally, normality and equality of variances were checked by Shapiro-Wilk and Levene's test, respectively.

3. Results

3.1. Compressive tests in solid cubes and isotropy analysis

To test for different mechanical properties along different directions in samples manufactured in both FFF printers. Solid cubes were printed and assessed in compressive tests in three different defined axes (Fig. 1). It was observed that the E_{app} was significantly higher for both FFF printers in the Z axis, while both the X and Y axes showed similar values within printers (transverse isotropy). The In-House FFF printer showed a significantly higher E_{app} when compared with the commercial printer in all axes. Regarding the Yield stress, though the In-House also showed higher values than the commercial printer in all axes, the commercial printer showed similar Yield stress responses within the three different axes, behaving as an isotropic structure in regard to this property (Fig. 2).

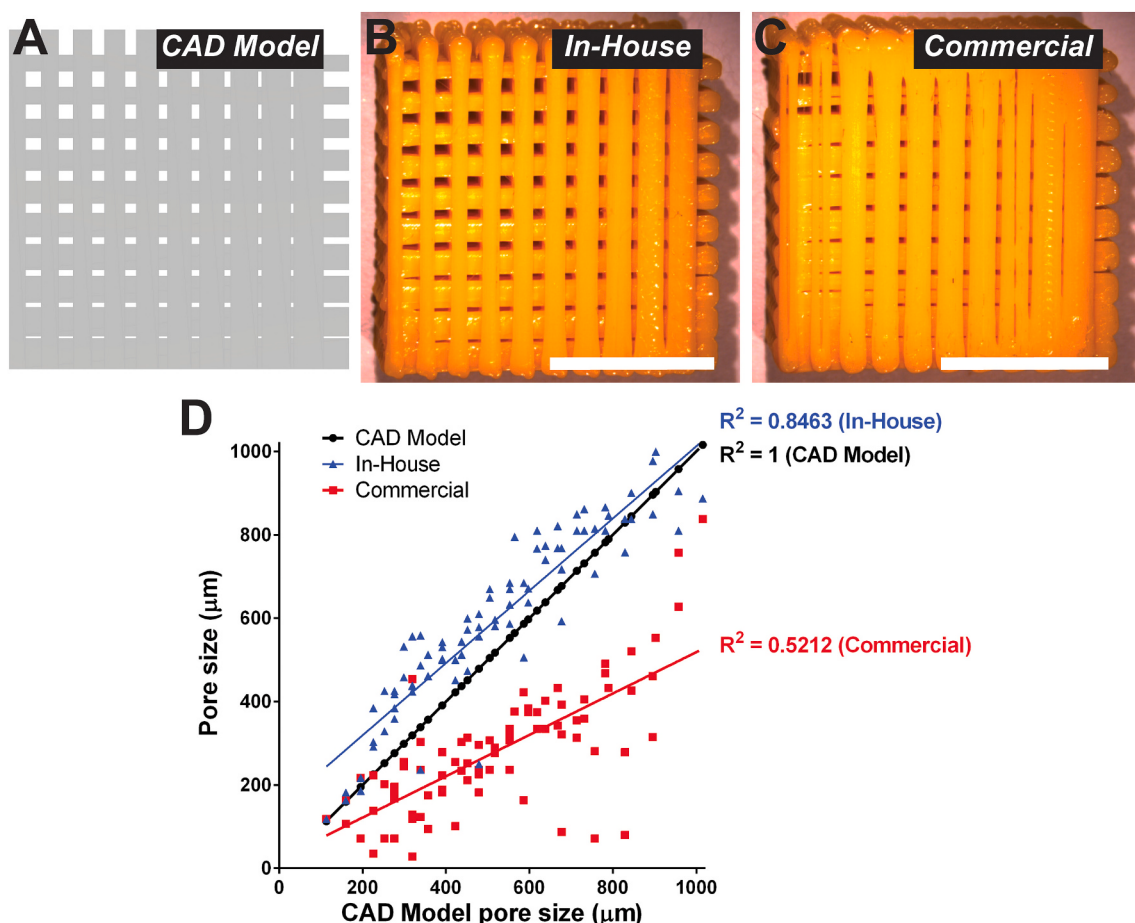


Fig. 3. The In-House FFF printer shows better pore resolution than the commercial one after manufacturing a porous structure. (A) CAD Model of a porous structure with 81 pores of variable areas. (B) Porous structure manufactured in the In-House FFF printer. (C) Porous structure manufactured in the commercial FFF printer. (D) Quantification of all pore sizes in both structures in comparison with the CAD Model, The CAD model is also included as a control for the ideal structure (line with $R^2 = 1$). The scale bars in (B) and (C) represent 1 cm.

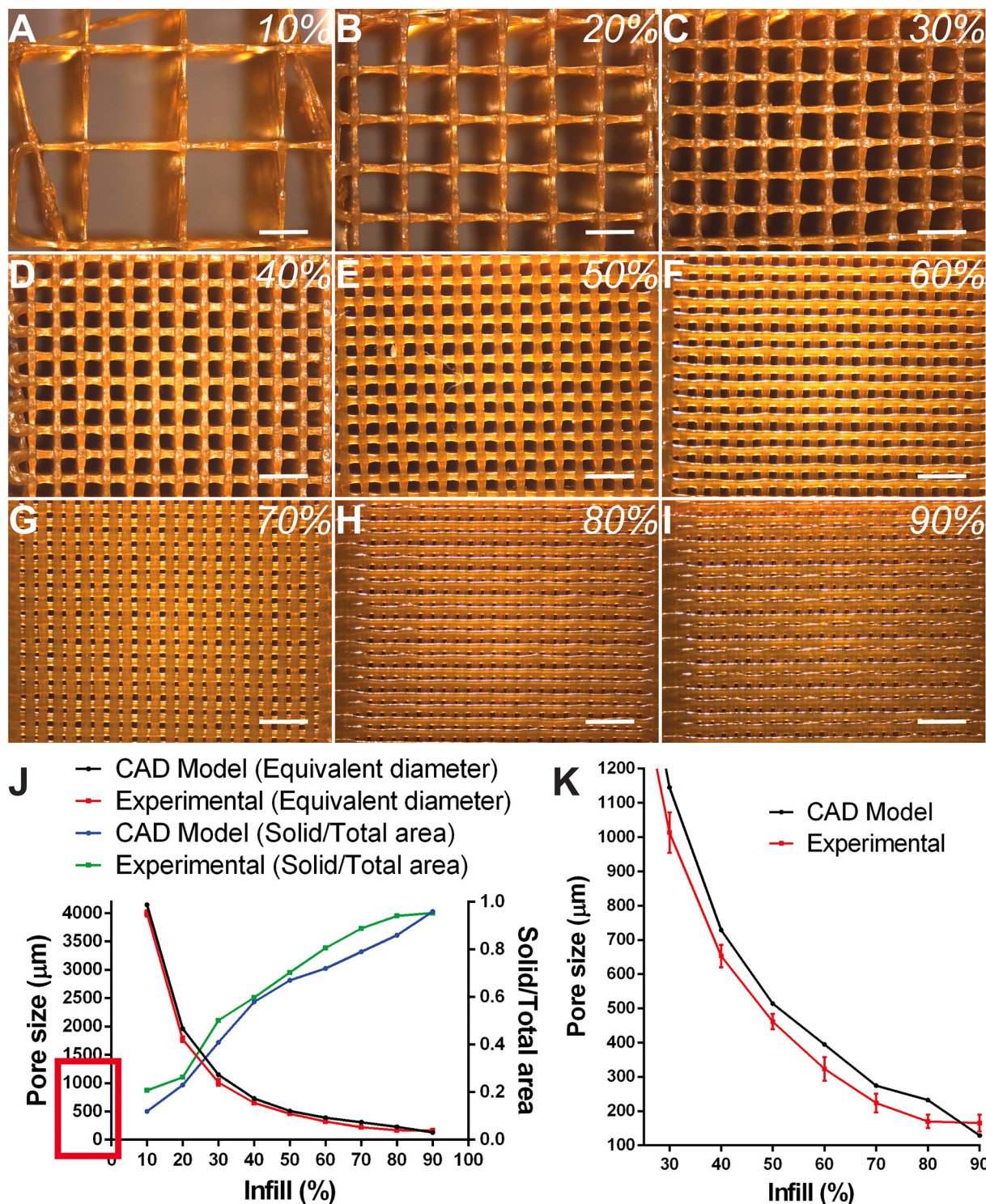


Fig. 4. The In-House FFF printer achieves small pore sizes at high infill densities. (A to I) Cubic samples manufactured from 10 to 90% infill density, scale bars represent 2 mm. (J) Quantification of both the equivalent diameter and the ratio between solid to total area of each panel shown in (A to I) between the In-House and the theoretical CAD model. (K) Magnification of the equivalent diameter axis from (J) in the micron scale from 100 to 1200 μm (also comparing the In-House with the CAD model). Each point represents the mean with the SD.

3.2. Microarchitectural and resolution comparison between FFF printers

To compare the ability of each FFF printer to achieve high resolution to manufacture a structure with pores of variable areas, a CAD Model was designed which consisted in struts of variable spacing with external dimensions of $21 \times 21.02 \times 3$ mm, allowing for the creation of 81 pores which ranged in areas from 0.81 mm^2 to 0.01 mm^2 (Fig. 3A). After manufacturing this structure in PLA in both the In-House and commercial FFF printers, it was observed that the In-House achieved higher resolution and was able to prevent the occlusion of the pores even in the ones with the smallest areas. After quantifying the area of each pore, the equivalent pore size was calculated and compared with the pore size in each pore of the CAD model. It was observed that the In-House FFF printer accomplished a better fit to the theoretical values (Fig. 3).

3.3. Infill effect on pore size in the In-House FFF printer

To explore the resolution limits of the In-House FFF printer, a cube of $15 \times 15 \times 15$ mm was manufactured with variation in its infill from 10 to 90% (Fig. 4). The infill is a percentage that represents the ratio of solid material to the total volume of the structure, being a 100% infill a fully solid element. It has been shown that variation in this property can affect the mechanical behavior of 3D-printed parts, such as their tensile strength [20] and their dimensional accuracy [33], among others. The results show that at 90% infill, the In-House FFF printer was able to achieve pores with a pore size smaller than $200 \mu\text{m}$ (Fig. 4 Panel K), suggesting its high resolution capacity by FFF technology and its feasibility of use for cellular *in vitro* studies [8].

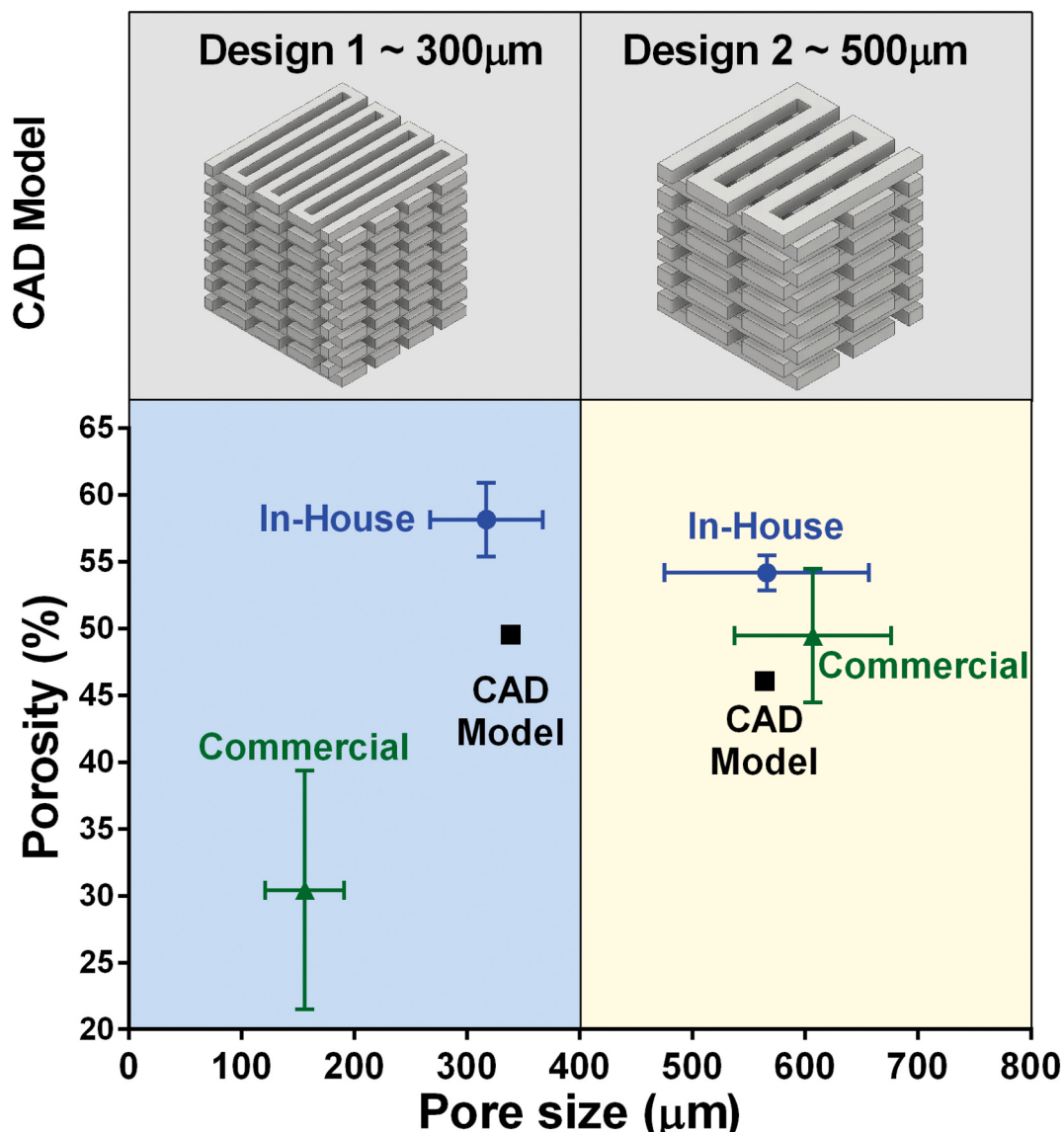


Fig. 5. The In-House FFF printer achieves better resolution than the commercial one when manufacturing small pore size scaffolds. The graph shows the pore size and porosity values for the commercial (green triangle), In-House (blue circle) and the CAD model of each corresponding Design (black square). Error bars represent the SD. (For interpretation of the references to colour in this figure legend, the reader is referred to the web version of this article.)

3.4. Microarchitectural assessment in porous scaffolds between FFF printers

After manufacturing both scaffolds (Designs 1 and 2) in both FFF printers, a microarchitectural characterization was performed in terms of their pore size and porosity. The results show that the In-House FFF printer was able to achieve characteristics closer to the corresponding CAD models (theoretical values) than its commercial counterpart with the Design 1 scaffold, while the Design 2 scaffold in the commercial printer showed a higher variability in porosity and a mean pore size bigger than the In-House (Fig. 5).

3.5. Mechanical analysis in porous scaffolds between FFF printers

To test the mechanical performance of porous scaffolds manufactured in both FFF printers, compression assays were done in porous scaffold of both pore size designs. The E_{app} of the In-House scaffolds showed no significant difference between them. Conversely, the Design 2 pore size commercial scaffold was significantly lower than its Design 2

pore size counterpart. Additionally, the E_{app} of the FEA models were in the range of those obtained experimentally fabricated by the In-House 3D printer (Fig. 6).

3.6. Cell adhesion efficiency in scaffolds manufactured in the in-house FFF printer

To address the feasibility of the In-House FFF printer to be used in biological experiments for tissue engineering applications, a preliminary biological assessment was performed to measure cell adhesion efficiency. The results show that both scaffold designs show similar values with efficiencies close to 50% of the control (Fig. 7). The Design 1 pore size scaffold showed an average efficiency of 50.31% ($SD = 6.38$), while the Design 2 pore size scaffold showed an average efficiency of 49.30% ($SD = 0.62$) (Fig. 6). Furthermore, the blank controls showed a small background signal with no significant differences among conditions, suggesting that the PLA scaffolds *per se* did not affect the measurement (OD of approximately 0.3 for all samples, data not shown).

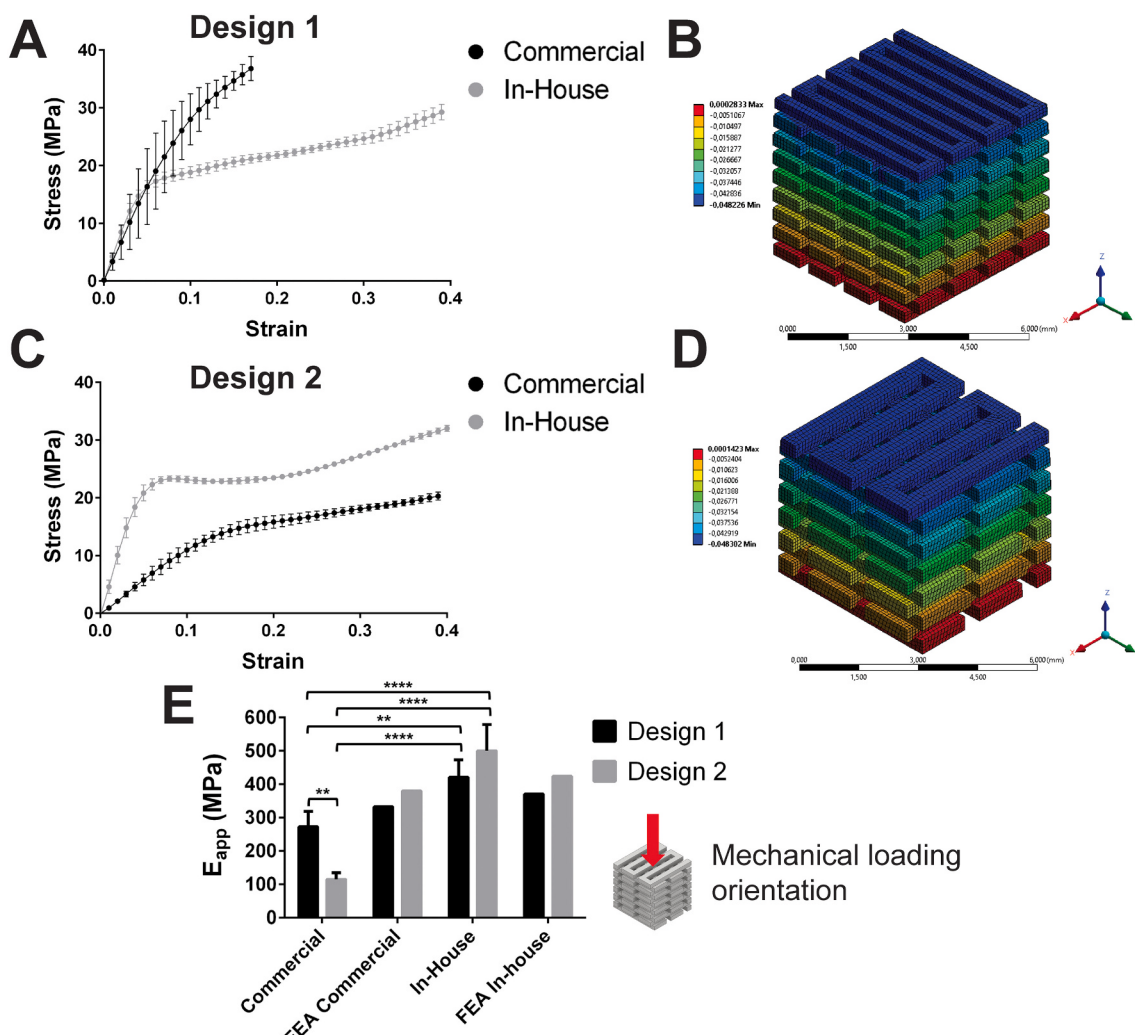


Fig. 6. The E_{app} of the In-House FFF printer scaffolds are closer to their FEA models than their commercial counterparts. (A) Stress strain curve of the Design 1 scaffold in both printers, each point represents the mean with the SD. (B) Example of FEA distribution of z-axis displacement for the Design 1 scaffold. (C) Stress strain curve of the Design 2 scaffold in both printers, each point represents the mean with the SD. (D) Example of FEA distribution of z-axis displacement for the Design 2 scaffold. (E) E_{app} of all samples including their FEA models. All samples were assayed in the same orientation (shown in the inset in E). Brackets represent statistical significance in a post-hoc Tukey test after ANOVA (* = $p < 0.05$, ** = $p < 0.01$, *** = $p < 0.001$, **** = $p < 0.0001$).

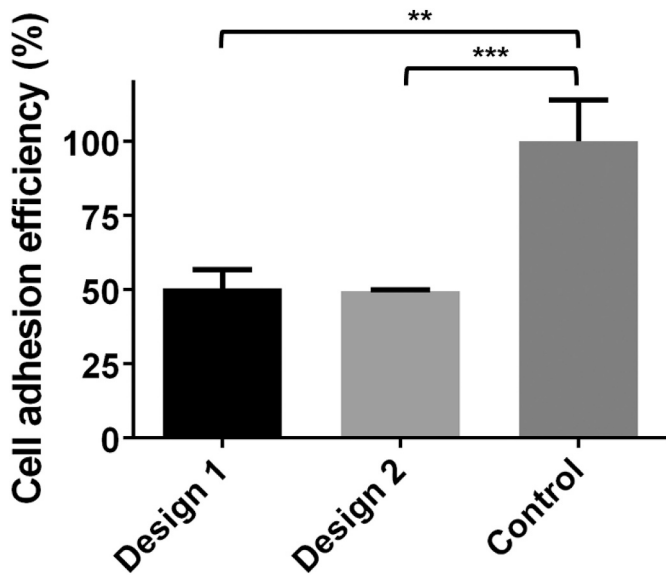


Fig. 7. hGMSCs show similar cell adhesion efficiency for both scaffolds manufactured in the In-House FFF printer. Cell adhesion efficiency for the Design 1 and Design 2 scaffolds in comparison with the control. Bar graphs indicate the mean with the SD in all cases ($n = 3$). Brackets represent statistical significance in a post-hoc Tukey test after ANOVA (* = $p < 0.05$, ** = $p < 0.01$, *** = $p < 0.001$, **** = $p < 0.0001$).

3.7. FTIR-ATR spectra of the PLA filament before and after extrusion in both printers

To understand if the PLA polymer suffered chemical changes due to the thermic process during FFF in each 3D printer, FTIR-ATR was performed for both printers, using the PLA as received as a control. The spectra were compared to each other, as well as PLA spectra reported in the literature [71,72]. The results show that the material did not suffer substantial changes in its spectra after extrusion in each 3D printer (Fig. 8).

4. Discussion

In this study, two FFF printers were used to analyze mechanical and geometrical properties of 3D-printed structures, as well as the resolution limits of our In-House 3D-Printer. Moreover, an assessment of its feasibility of use for tissue engineering applications was performed.

By doing compression tests in solid cubes in three different orientations, it was observed that the samples showed transverse isotropy in the X-Y axes, presenting a larger E_{app} in their default Z-orientation (Figs. 1 and 2). This trend has also been observed in other studies, for example, PLA structures manufactured by FFF were tougher when loaded in the extrusion direction than in the transverse one, according to compressive tests in cubes of side length 7 mm, and tensile tests in “flat dog bone” specimens [73]. More generally, structures manufactured by FFF show the largest mechanical anisotropy of all printing technologies [2,74], so the results observed in this study show an expected trend.

In this study, PLA was used as a study model. As mentioned earlier, this polymer has been widely used in tissue engineering for bone [2,53] and for orthopedic applications [54]. Some of its many advantages are its low-cost, biodegradability and biocompatibility, leading it to the

approval by the Food and Drug Administration (FDA) as a material for several biomedical applications [55]. By using PLA, some studies have performed not only geometrical and mechanical experiments [23,33], but also several biological evaluations [34,36,51].

By designing and manufacturing a porous structure with 81 pores that ranged in areas from 0.81 mm^2 to 0.01 mm^2 , it was observed that our In-House FFF printer reached a better fit to the expected theoretical values than its commercial counterpart (Fig. 3). Additionally, by varying the infill pattern of an otherwise solid sample, from 10 to 90%, pore sizes as small as $200 \mu\text{m}$ in diameter or less were achieved (Fig. 4). These experiments highlight the importance of not only controlling the architecture of a desired CAD Model, but also to achieve such design during fabrication. Although there is no definite consensus on the optimal pore size for cellular physiological activity, evidence in bioceramics for example suggests that a range from $100 \mu\text{m}$ to $1200 \mu\text{m}$ can become biologically relevant, both *in vitro* and *in vivo*, for parameters such as cell ingrowth, bone formation and bone regeneration [8,75–77]. Moreover, by assessing the performance of the in-house printer, Fig. 3 clearly showed that the in-house printer was able to print with a higher fidelity and reliability over a wide range of pore sizes compared to the *low cost* commercially available printer.

In this study, porous scaffolds of $300 \mu\text{m}$ (Design 1) and $500 \mu\text{m}$ (Design 2) pore size, with porosity close to 50% were used as models to assess the manufacturing process and its variability, by assessing microarchitectural parameters like pore size and porosity. Other studies have also used similar structures for similar purposes, for example by using pores in the range of 300 – $700 \mu\text{m}$, and porosities in the range of 50% [34,36]. For an updated literature review characterizing the designed and obtained microarchitectural parameters of PLA-based scaffolds during FFF manufacturing, see Table 1. For a specific comparison of the designed and obtained pore size from the literature, see Fig. 9, in which it can be observed that the In-House generally presents a more consistent resolution than its commercial counterpart.

In this study, a mechanical analysis by means of compressive tests was performed, additionally, numerical simulation by FEA was conducted to compare the experimental results with an expected theoretical model. This approach has been used previously in the literature [26,27], given that it allows to address their manufacture variability. As expected, and based on the microarchitectural comparison, the In-House scaffolds showed a more consistent mechanical response according to their E_{app} than their commercial counterparts, obtaining values closer to their FEA models (Fig. 6). From all conditions, the Design 2 scaffolds in the commercial were farthest from their FEA models, which should have been more than twice larger.

By normalizing the E_{app} of the scaffolds with the elastic modulus of the solid cubes (E_0), it can be observed that the added porosity decreases the E_{app} of these structures. This trend has been widely reported in the literature by different mathematical models that show the E_{app}/E_0 as a function of porosity in artificial porous structures fabricated by additive manufacturing [78–85], this becomes a relevant comparison, given that our results can be contrasted with these models. Interestingly, the scaffolds used in this study fall within the range of expected responses according to their porosities, with the In-House scaffolds closer to their corresponding FEA models, suggesting its lower variability (Fig. 10). The geometrical resolution obtained in a 3D-scaffold and its repeatability is of absolute relevance not only to have a consistent mechanical response, but also to guarantee that cells within a biological context will react in a predictable way during tissue engineering applications, given that they sense the micromechanical local environment [25].

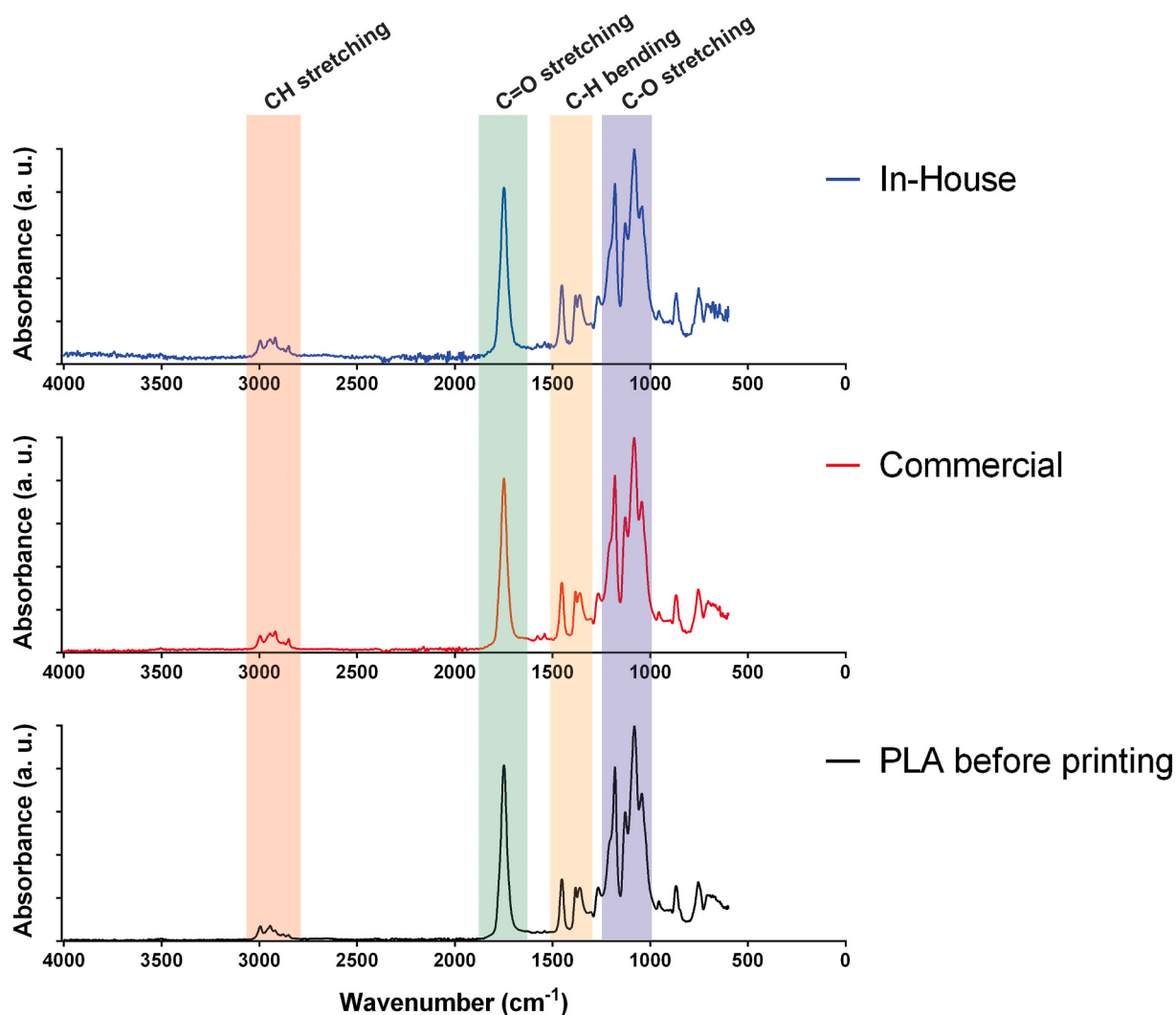


Fig. 8. The PLA presents no substantial changes in its FTIR-ATR spectra after extrusion in both 3D printers. FTIR-ATR spectra of the PLA filament after extrusion in the In-House (blue) and the Commercial printer (red), using the PLA filament before extrusion as a control (black). The main signatures are shown, based on [71]. (For interpretation of the references to colour in this figure legend, the reader is referred to the web version of this article.)

Among many additive manufacturing available approaches for tissue engineering applications, FFF is a suitable candidate, given that it is a fast, simple, and low cost [12]. Also, it allows for a rather complete repertoire of *in vitro* biological assessments in 3D-porous scaffolds. For example, the addition of polymeric or ceramic coatings can enhance the biocompatibility of PLA scaffolds, improving properties like cell attachment, proliferation and differentiation [36,86]. Additionally, PLA can be used as a matrix to test the biological response to composite materials [47].

In this study, a preliminary biological assessment was performed in terms of cell adhesion efficiency, which means the fraction of cells that attach to a scaffold after a certain period of time. This biological property becomes most relevant if the goal of 3D-scaffolds is to be loaded with cells from a patient, stimulated mechanically or chemically, and then implanted for tissue regeneration therapies [87]. Our results show that hGMSCs reached an adhesion efficiency in both scaffold designs of approximately 50% after one day in culture conditions (Fig. 6). These

values are close to experiments performed in similar conditions, for example, by using PLA-based composite scaffolds fabricated with a nozzle-based rapid prototyping system, an adhesion efficiency (named as “adhesion” in the study) of approximately 60% was achieved by using rat mesenchymal stem cells after either 4 or 24 h in culture conditions [51]. Similarly, by using the related polymer poly(l-lactic acid) (PLLA), and fabricating films and porous membranes of different thicknesses by a freeze-extraction and particle leaching method [88], an adhesion efficiency (named as “adherence” in the study) of approximately 40% was achieved in films and membranes of 100 and 200 μm thickness, with the 300 μm thickness membrane showing the highest value of about 70%, according to experiments performed with human bone marrow-derived MSCs after 3 h in culture conditions [70].

To address whether the PLA filament suffered chemical changes after 3D printing, FTIR-ATR experiments were performed, and the spectra obtained was compared with PLA spectra obtained from the literature

Table 1

Literature review of the designed and obtained microarchitectural parameters of PLA-based scaffolds during FFF manufacturing (NR = not reported).

Author	Architectural characteristic	Material	Porosity (%)		Pore size (μm)	
			Design	Exp	Design	Exp
Grémare et al., 2018 [90]	Controlled pore size	PLA	NR	NR	150 200 250	138 \pm 13 190 \pm 11 237 \pm 14
Donate et al., 2020 [47]	Controlled porosity	PLA	50	54.7 \pm 2.2	350–450	421.45 \pm 54.53
		PLA:CaCO ₃ 95:5	50	58.6 \pm 1.5	350–450	424.61 \pm 51.49
		PLA: β -TCP 95:5	50	58.8 \pm 0.8	350–450	396.64 \pm 29.86
		PLA:CaCO ₃ : β -TCP 95:2.5:2.5	50	58.3 \pm 3.6	350–450	410.99 \pm 48.24
Pecci et al., 2020 [53]	Random microarchitecture	PLA	27% (porogen size of 400 μm)	23.25–28.17	400	NR
			46% (porogen size of 500 μm)	38.26–44.16	500	
			65% (porogen size of 600 μm)	60–60.34	600	
			35% (porogen size of 400–600 μm)	29.23–33	400–600	
Gendviliene et al., 2020 [19]	Controlled pore size and porosity	PLA 1	48	25.17 (retrieved average) (gravimetric method) 29.27 (retrieved average) (liquid displacement method)	400	341.95 (retrieved median)
		PLA 2	48	67.84 (retrieved average) (gravimetric method) 48.86 (retrieved average) (liquid Displacement method)	400	398.30 (retrieved median)
		PLA/Hap	48	48.15 \pm 0.01 (gravimetric method) 50.6 \pm 0.06 (liquid displacement method)	400	349.78 (retrieved median)
Germain et al., 2018 [55]	Gyroid scaffolds (with regular scaffolds as controls)	PLA (amorphous and semi-crystalline)	73.7	70.8 (SD = 0.5) (from mass and dimensions method) 74.7 (from μCT scan images method)	NR	NR
Teixeira et al., 2018 [36]	Controlled pore size	PLA with polydopamine and type I collagen coating	NR	60 \pm 1.5	0.3 mm (lateral side) and 0.7 mm (surface and bottom)	NR
Souness et al., 2017 [91]	Controlled pore size and porosity	PLA with pullulan and hyaluronic acid coatings	25.86 (retrieved from graph)	28.8 \pm 0.9	400 \times 400 (0°/90° deposition angle) (single)	311.9 \pm 9.57 \times 266.89 \pm 7.66
			25.86 (retrieved from graph)	28.9 \pm 1.0	400 \times 400 (0°/90° deposition angle) (double)	329.65 \pm 20.1 \times 245.98 \pm 17.99
			46.01 (retrieved from graph)	35.7 \pm 2.4	600 \times 600 (45°/135° deposition angle)	479.01 \pm 13.77 \times 346.49 \pm 12.86
			43.21 (retrieved from graph)	38.8 \pm 0.3	600 \times 600 (60°/120° deposition angle)	462.91 \pm 4.54 \times 336.38 \pm 16.91
			37.50 (retrieved from graph)	33.8 \pm 1.0	500 \times 500 (0°/90° deposition angle)	318.42 \pm 20.39 \times 243.32 \pm 13.16
			13.14 (retrieved from graph)	17.0 \pm 0.8	600 \times 800 (no deposition angle)	528.95 \pm 15.08 \times 254.65 \pm 23.76
			\approx 30 (Model ST1)	31 (mean with SD = 4)	350	NR
			\approx 50 (Model ST2)	52 (mean with SD = 3)	700	
Syuhada et al., 2018 [5]	Controlled pore size and porosity	PLA with hydroxyapatite and alginate filler	61.5% (3 layers scaffold)	55.3% (mean) (without filler)	0.81 (mm^2)	0.80 (SD = 0.03) (mm^2) (axial direction)
			61.5% (4 layers scaffold)	51.7% (mean) (without filler)	0.81 (mm^2)	0.99 (SD = 0.06) (mm^2) (axial direction)
			61.5% (6 layers scaffold)	62.3% (mean) (without filler)	0.81 (mm^2)	0.92 (SD = 0.03) (mm^2) (axial direction)
Jaidev & Chatterjee, 2019 [86]	Controlled pore size and porosity	PLA with hydroxyapatite coating	NR	70.2	500	314 \pm 58
This study	Controlled pore size and porosity	PLA	49.56 (300 μm pore size)	58.14 (SD = 2.76) (In-House printer) 30.43 (SD = 8.94) (Commercial printer)	339	317.18 (SD = 50.07) (In-House printer) 156.14 (SD = 35.02) (Commercial printer)

(continued on next page)

Table 1 (continued)

Author	Architectural characteristic	Material	Porosity (%)		Pore size (μm)	
			Design	Exp	Design	Exp
			46.08 (500 μm pore size)	54.17 (SD = 1.30) (In-House printer) 49.45 (SD = 5.00) (Commercial printer)	564	565.89 (SD = 90.64) (In-House printer) 606.84 (SD = 69.47) (Commercial printer)

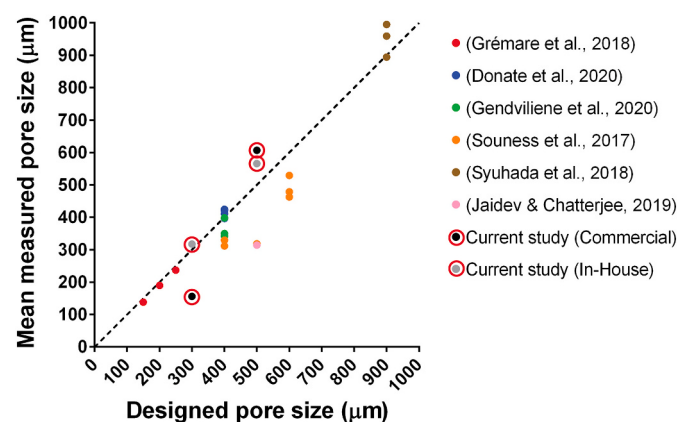


Fig. 9. Designed and obtained pore sizes in porous scaffolds by FFF manufacturing of PLA structures. The dotted line represents the $X = Y$ diagonal. All points represent the average of the measurement, except for Gendviliene et al., which shows the median. Note that the In-House mean measured pore sizes are closer to their theoretical expected values.

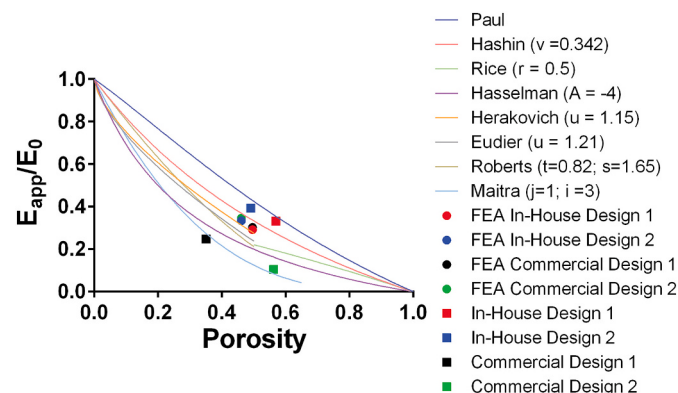


Fig. 10. Models of the E_{app}/E_0 as a function of porosity in artificial porous structures (based on [78]). The mean values for both scaffolds and FEA models are shown. Note that our results fall within the range of models from the literature, with the In-House FEA models closer to their experimental results.

[48,71]. We observed a spectrum that is consistent with the reported one in the literature for this polymer, showing for example a characteristic peak of $\text{C}=\text{O}$ stretching between 1500 and 2000 (wavenumber), as well as small -CH stretching peaks near 3000 (wavenumber), among others (Fig. 8). Furthermore, all three conditions presented a similar spectrum, suggesting that the material did not suffer substantial chemical changes after extrusion in each 3D printer. Future experiments can address this question with composite materials that use PLA as a matrix in our In-House 3D printer, given that this procedure does alter FTIR spectra [48].

Taken together, the above-mentioned results and their comparison with the literature highlights the relevance of understanding the complex link between scaffold architecture with their mechanical and biological performance, given that this relationship is valuable for the tissue engineering field [89].

5. Conclusions

We have investigated the manufacture of both solid and porous PLA samples in our In-House FFF printer, using a commercial desktop equivalent counterpart for comparison purposes. In particular, we manufactured solid cubes and assayed them by compression tests in three different orientations, the results show that the In-House samples present not only a significantly higher elastic modulus than the commercial-made ones, but also different orientations presented different yield stress responses in samples manufactured in the In-House, which was not observed in the commercial counterpart. By comparing a porous structure with microarchitecture manufactured in both printers, it was observed that the In-House achieved better resolution, according to how close the obtained pore sizes were to their corresponding CAD models. Accordingly, an infill analysis showed that the In-House can achieve pore size resolutions in the order of 100–200 μm .

By manufacturing scaffolds of both pore sizes, a design suitable to use in tissue engineering, it was observed that the In-House FFF printer was able to achieve characteristics that are generally closer to the corresponding CAD models. Furthermore, compression tests in these scaffolds showed that the In-House achieved E_{app} values closer to their FEA models and significantly higher than their commercial-made counterparts. Additionally, a preliminary biological assessment for cell adhesion efficiency in these scaffolds, manufactured in the In-House printer, show that it is possible to obtain adhesion efficiencies close to what is observed in the literature with similar methodologies. Finally, FTIR-ATR spectra analysis show that the PLA polymer did not suffer substantial chemical changes after extrusion in each 3D printer.

This study shows that our low-cost, open-source In-House FFF printer is a cost-effective approach to manufacture tissue engineering scaffolds, which allows to explore the association between structure and function, as well as their relationship with both the mechanical and biological performance in 3D-porous scaffolds. Therefore, future studies will make use of this printer loaded with different materials to perform mechanical and biological assessments that will contribute to hard tissue regeneration research.

CRediT authorship contribution statement

Raúl Vallejos: Methodology, Validation, Investigation, Writing - Original Draft, Writing - Review & Editing, Visualization. **José Contreras:** Software, Validation, Formal analysis, Investigation. **Carlos Toro:** Validation, Formal analysis, Investigation. **Miguel Bustamante:** Validation, Formal analysis, Visualization. **Luis Pérez:** Methodology, Software, Formal analysis, Visualization. Luis Pérez: Methodology, Validation, Writing- Review & Editing. **Lurii Burda:** Methodology, Investigation, Visualization. **Ameet Aiyangar:** Writing - Review & Editing, Supervision, Visualization. **Juan F. Vivanco:** Conceptualization, Writing - Review & Editing, Visualization, Supervision, Project administration, Funding acquisition.

Declaration of competing interest

The authors declare no conflict of interest.

Acknowledgements

This research was funded by “Agencia Nacional de Investigación y Desarrollo” (ANID) from the Government of Chile, through the Research Project FONDECYT Inicio” N° 11170957. The authors also thank the Research Seed Funds Program (RSF) within the framework of the Engineering 2030 initiative from “Facultad de Ingeniería y Ciencias, Universidad Adolfo Ibáñez” (FIC-UAI). R.V. thanks “Universidad Adolfo Ibáñez” for providing postdoctoral funding. The authors would also like to thank Ms. Olga Sambalova for assistance with the FTIR-ATR measurements.

Appendix A. Supplementary data

The STL files to manufacture the cubic mold for scaffold cell seeding, as well as the porous samples used in this study, are available for download in the supplementary materials. Supplementary data to this article can be found online at doi:<https://doi.org/10.1016/j.msec.2021.1111945>.

References

- [1] A.J. Wagoner Johnson, B.A. Herschler, A review of the mechanical behavior of CaP and CaP/polymer composites for applications in bone replacement and repair, *Acta Biomater.* 7 (2011) 16–30, <https://doi.org/10.1016/j.actbio.2010.07.012>.
- [2] X. Chen, G. Chen, G. Wang, P. Zhu, C. Gao, Recent progress on 3D-printed poly(lactic acid) and its applications in bone repair, *Adv. Eng. Mater.* 22 (2020), <https://doi.org/10.1002/adem.201901065>.
- [3] E. Nyberg, A. Rindone, A. Dorafshar, W.L. Grayson, Comparison of 3D-printed poly-ε-caprolactone scaffolds functionalized with tricalcium phosphate, hydroxyapatite, bio-oss, or decellularized bone matrix, *Tissue Eng. A* 23 (2017) 503–514, <https://doi.org/10.1089/ten.tea.2016.0418>.
- [4] Q.L. Loh, C. Choong, Three-dimensional scaffolds for tissue engineering applications: role of porosity and pore size, *Tissue Eng. B Rev.* 19 (2013) 485–502, <https://doi.org/10.1089/ten.teb.2012.0437>.
- [5] G. Syuhada, G. Ramahdita, A.J. Rahyussalim, Y. Whulanza, Multi-material Poly (Lactic Acid) Scaffold Fabricated via Fused Deposition Modeling and Direct Hydroxyapatite Injection as Spacers in Laminoplasty, *AIP Conf. Proc.* 2018, p. 020008, <https://doi.org/10.1063/1.5023942>.
- [6] A. Kehinde Aworinde, S. Oluropo Adeosun, F. Adekunle Oyawale, E. Titilayo Akinlabi, S.A. Akinlabi, Parametric effects of fused deposition modelling on the mechanical properties of polylactide composites: a review, *J. Phys. Conf. Ser.* 1378 (2019) 022060, <https://doi.org/10.1088/1742-6596/1378/2/022060>.
- [7] S.J. Hollister, Porous scaffold design for tissue engineering, *Nat. Mater.* 4 (2005) 518–524, <https://doi.org/10.1038/nmat1421>.
- [8] V. Karageorgiou, D. Kaplan, Porosity of 3D biomaterial scaffolds and osteogenesis, *Biomaterials.* 26 (2005) 5474–5491, <https://doi.org/10.1016/j.biomaterials.2005.02.002>.
- [9] S.F. Hulbert, F.A. Young, R.S. Mathews, J.J. Klawitter, C.D. Talbert, F.H. Stelling, Potential of ceramic materials as permanently implantable skeletal prostheses, *J. Biomed. Mater. Res.* 4 (1970) 433–456, <https://doi.org/10.1002/jbm.820040309>.
- [10] A.I. Itl, H.O. Ylnen, C. Ekholm, K.H. Karlsson, H.T. Aro, Pore diameter of more than 100 µm is not requisite for bone ingrowth in rabbits, *J. Biomed. Mater. Res.* 58 (2001) 679–683, <https://doi.org/10.1002/jbm.1069>.
- [11] S. Sánchez-Salcedo, D. Arcos, M. Vallet-Regí, Upgrading calcium phosphate scaffolds for tissue engineering applications, *Key Eng. Mater.* 377 (2008) 19–42, <https://doi.org/10.4028/www.scientific.net/KEM.377.19>.
- [12] T.D. Ngo, A. Kashani, G. Imbalzano, K.T.Q. Nguyen, D. Hui, Additive manufacturing (3D printing): a review of materials, methods, applications and challenges, *Compos. Part B* 143 (2018) 172–196, <https://doi.org/10.1016/j.compositesb.2018.02.012>.
- [13] A. Velasco-Hogan, J. Xu, M.A. Meyers, Additive manufacturing as a method to design and optimize bioinspired structures, *Adv. Mater.* 30 (2018) 1–26, <https://doi.org/10.1002/adma.201800940>.
- [14] K.A. Deo, K.A. Singh, C.W. Peak, D.L. Alge, A.K. Gaharwar, Bioprinting 101: design, fabrication, and evaluation of cell-laden 3D bioprinted scaffolds, *Tissue Eng. Part A* 26 (2020) 318–338, <https://doi.org/10.1089/ten.tea.2019.0298>.
- [15] J.A. Semba, A.A. Mieloch, J.D. Rybka, Introduction to the state-of-the-art 3D bioprinting methods, design, and applications in orthopedics, *Bioprinting.* 18 (2020), e00070, <https://doi.org/10.1016/j.bprint.2019.e00070>.
- [16] W. Wang, K.W.K. Yeung, Bone grafts and biomaterials substitutes for bone defect repair: a review, *Bioact. Mater.* 2 (2017) 224–247, <https://doi.org/10.1016/j.bioactmat.2017.05.007>.
- [17] J.K. Placome, B. Mahadik, J.P. Fisher, Addressing present pitfalls in 3D printing for tissue engineering to enhance future potential, *APL Bioeng.* 4 (2020), 010901, <https://doi.org/10.1063/1.5127860>.
- [18] D. Popescu, A. Zapciu, C. Amza, F. Baciu, R. Marinescu, FDM process parameters influence over the mechanical properties of polymer specimens: a review, *Polym. Test.* 69 (2018) 157–166, <https://doi.org/10.1016/j.polymertesting.2018.05.020>.
- [19] I. Gendvilienė, E. Simoliūnas, S. Rekštystė, M. Malinauskas, L. Zaleckas, D. Jegelevicius, V. Bukelskiene, V. Rutkunas, Assessment of the morphology and dimensional accuracy of 3D printed PLA and PLA/HAp scaffolds, *J. Mech. Behav. Biomed. Mater.* 104 (2020), 103616, <https://doi.org/10.1016/j.jmbbm.2020.103616>.
- [20] M. Fernandez-Vicente, W. Calle, S. Ferrandiz, A. Conejero, Effect of infill parameters on tensile mechanical behavior in desktop 3D printing, *3D print. Addit. Manuf.* 3 (2016) 183–192, <https://doi.org/10.1089/3dp.2015.0036>.
- [21] S.M. Lebedev, O.S. Gefle, E.T. Amitov, D.V. Zhuravlev, D.Y. Berchuk, E. A. Mikutskiy, Mechanical properties of PLA-based composites for fused deposition modeling technology, *Int. J. Adv. Manuf. Technol.* 97 (2018) 511–518, <https://doi.org/10.1007/s00170-018-1953-6>.
- [22] C. Pagano, L. Rebaioli, F. Baldi, I. Fassi, Relationships between size and mechanical properties of scaffold-like structures, *Mech. Adv. Mater. Struct.* 0 (2020) 1–6, <https://doi.org/10.1080/15376494.2019.1709675>.
- [23] J.M. Chacón, M.A. Caminero, E. García-Plaza, P.J. Núñez, Additive manufacturing of PLA structures using fused deposition modelling: effect of process parameters on mechanical properties and their optimal selection, *Mater. Des.* 124 (2017) 143–157, <https://doi.org/10.1016/j.matdes.2017.03.065>.
- [24] S. Gerdes, A. Mostafavi, S. Ramesh, A. Memic, I.V. Rivero, P. Rao, A. Tamayol, Process-structure-quality relationships of three-dimensional printed poly (caprolactone)-hydroxyapatite scaffolds, *Tissue Eng. Part A* 26 (2020) 279–291, <https://doi.org/10.1089/ten.tea.2019.0237>.
- [25] A. Campos Marin, D. Lacroix, The inter-sample structural variability of regular tissue-engineered scaffolds significantly affects the micromechanical local cell environment, *Interface Focus* 5 (2015) 20140097, <https://doi.org/10.1098/rsfs.2014.0097>.
- [26] B. Zhang, L. Guo, H. Chen, Y. Ventikos, R.J. Narayan, J. Huang, Finite element evaluations of the mechanical properties of polycaprolactone/hydroxyapatite scaffolds by direct ink writing: effects of pore geometry, *J. Mech. Behav. Biomed. Mater.* 104 (2020), 103665, <https://doi.org/10.1016/j.jmbbm.2020.103665>.
- [27] C. Sandino, J.A. Planell, D. Lacroix, A finite element study of mechanical stimuli in scaffolds for bone tissue engineering, *J. Biomech.* 41 (2008) 1005–1014, <https://doi.org/10.1016/j.jbiomech.2007.12.011>.
- [28] F.P.W. Melchels, K. Bertoldi, R. Gabbielli, A.H. Velders, J. Feijen, D.W. Grijpma, Mathematically defined tissue engineering scaffold architectures prepared by stereolithography, *Biomaterials.* 31 (2010) 6909–6916, <https://doi.org/10.1016/j.biomaterials.2010.05.068>.
- [29] W.J. Hendrikson, A.J. Deegan, Y. Yang, C.A. van Blitterswijk, N. Verdonschot, L. Moroni, J. Rouwkema, Influence of additive manufactured scaffold architecture on the distribution of surface strains and fluid flow shear stresses and expected osteochondral cell differentiation, *Front. Bioeng. Biotechnol.* 5 (2017) 1–11, <https://doi.org/10.3389/fbioe.2017.00006>.
- [30] O.L. Rodríguez-Montaño, C.J. Cortés-Rodríguez, A.E. Uva, M. Fiorentino, M. Gattullo, G. Monno, A. Boccaccio, Comparison of the mechanobiological performance of bone tissue scaffolds based on different unit cell geometries, *J. Mech. Behav. Biomed. Mater.* 83 (2018) 28–45, <https://doi.org/10.1016/j.jmbbm.2018.04.008>.
- [31] P. Egan, Integrated design approaches for 3D printed tissue scaffolds: review and outlook, *Materials (Basel)* 12 (2019) 2355, <https://doi.org/10.3390/ma12152355>.
- [32] M.P. Walzik, V. Vollmar, T. Lachnit, H. Dietz, S. Haug, H. Bachmann, M. Fath, D. Aschenbrenner, S. Abolpour Mofrad, O. Friedrich, D.F. Gilbert, A portable low-cost long-term live-cell imaging platform for biomedical research and education, *Biosens. Bioelectron.* 64 (2015) 639–649, <https://doi.org/10.1016/j.bios.2014.09.061>.
- [33] G.W. Melenka, J.S. Schofield, M.R. Dawson, J.P. Carey, Evaluation of dimensional accuracy and material properties of the MakerBot 3D desktop printer, *Rapid Prototyp. J.* 21 (2015) 618–627, <https://doi.org/10.1108/RPJ-09-2013-0093>.
- [34] A. Gregor, E. Filová, M. Novák, J. Kronek, H. Chlup, M. Buzgo, V. Blahnová, V. Lukášová, M. Bartoš, A. Nečas, J. Hošek, Designing of PLA scaffolds for bone tissue replacement fabricated by ordinary commercial 3D printer, *J. Biol. Eng.* 11 (2017) 1–21, <https://doi.org/10.1186/s13036-017-0074-3>.
- [35] A.S. Alagoz, V. Hasirci, 3D printing of polymeric tissue engineering scaffolds using open-source fused deposition modeling, *Emergent Mater.* (2019), <https://doi.org/10.1007/s42247-019-00048-2>.
- [36] B.N. Teixeira, P. Aprile, R.H. Mendonça, D.J. Kelly, R.M. da, S.M. Thiré, Evaluation of bone marrow stem cell response to PLA scaffolds manufactured by 3D printing and coated with polydopamine and type I collagen, *J. Biomed Mater Res B Appl Biomater* 107 (2018) 37–49, <https://doi.org/10.1002/jbm.b.34093>.
- [37] J.A. Ramírez, V. Ospina, A.A. Rozo, M.I. Viana, S. Ocampo, S. Restrepo, N. A. Vásquez, C. Paucar, C. García, Influence of geometry on cell proliferation of PLA and alumina scaffolds constructed by additive manufacturing, *J. Mater. Res.* 34 (2019) 3757–3765, <https://doi.org/10.1557/jmr.2019.323>.
- [38] A. Moetazedian, A. Gleddall, X. Han, V.V. Silberschmidt, Effect of environment on mechanical properties of 3D printed polylactide for biomedical applications, *J. Mech. Behav. Biomed. Mater.* 102 (2020), 103510, <https://doi.org/10.1016/j.jmbbm.2019.103510>.
- [39] K. Aou, S.L. Hsu, L.W. Kleiner, F.W. Tang, Roles of conformational and configurational defects on the physical aging of amorphous poly(lactic acid), *J. Phys. Chem. B* 111 (2007) 12322–12327, <https://doi.org/10.1021/jp074509r>.
- [40] M. Guvendiren, J. Molde, R.M.D. Soares, J. Kohn, Designing biomaterials for 3D printing, *ACS Biomater Sci. Eng.* 2 (2016) 1679–1693, <https://doi.org/10.1021/acsbiomaterials.6b00121>.

- [41] D. da Silva, M. Kaduri, M. Poley, O. Adir, N. Krinsky, J. Shainsky-Roitman, A. Schroeder, Biocompatibility, biodegradation and excretion of poly(lactic acid) (PLA) in medical implants and therapeutic systems, *Chem. Eng. J.* 340 (2018) 9–14, <https://doi.org/10.1016/j.cej.2018.01.010>.
- [42] S. Farah, D.G. Anderson, R. Langer, Physical and mechanical properties of PLA, and their functions in widespread applications — a comprehensive review, *Adv. Drug Rev.* 107 (2016) 367–392, <https://doi.org/10.1016/j.addr.2016.06.012>.
- [43] K. Madhavan Nampoothiri, N.R. Nair, R.P. John, An overview of the recent developments in polylactide (PLA) research, *Bioresour. Technol.* 101 (2010) 8493–8501, <https://doi.org/10.1016/j.biortech.2010.05.092>.
- [44] S. Liu, S. Qin, M. He, D. Zhou, Q. Qin, H. Wang, Current applications of poly(lactic acid) composites in tissue engineering and drug delivery, *Compos. Part B* 199 (2020), 108238, <https://doi.org/10.1016/j.compositesb.2020.108238>.
- [45] C. Esposito Corcione, F. Gervaso, F. Scalera, F. Montagna, A. Sannino, A. Maffezzoli, The feasibility of printing poly(lactic acid)-nanohydroxyapatite composites using a low-cost fused deposition modeling 3D printer, *J. Appl. Polym. Sci.* 134 (2017) 1–10, <https://doi.org/10.1002/app.44656>.
- [46] D. Drummer, S. Cifuentes-Cuéllar, D. Rietzel, Suitability of PLA/TCP for fused deposition modeling, *Rapid Prototyp. J.* 18 (2012) 500–507, <https://doi.org/10.1108/13552541211272045>.
- [47] R. Donato, M. Monzón, Z. Ortega, L. Wang, V. Ribeiro, D. Pestana, J.M. Oliveira, R. L. Reis, Comparison between calcium carbonate and β-tricalcium phosphate as additives of 3D printed scaffolds with poly(lactic acid) matrix, *J. Tissue Eng. Regen. Med.* 14 (2020) 272–283, <https://doi.org/10.1002/term.2990>.
- [48] H. Belaid, S. Nagarajan, C. Teyssier, C. Barou, J. Barés, S. Balme, H. Garay, V. Huon, D. Cornu, V. Cavallès, M. Bechelany, Development of new biocompatible 3D printed graphene oxide-based scaffolds, *Mater. Sci. Eng. C* 110 (2020), 110595, <https://doi.org/10.1016/j.msec.2019.110595>.
- [49] H. Belaid, S. Nagarajan, C. Barou, V. Huon, J. Barés, S. Balme, P. Miele, D. Cornu, V. Cavallès, C. Teyssier, M. Bechelany, Boron nitride based nanobiocomposites: design by 3D printing for bone tissue engineering, *ACS Appl. Bio Mater.* 3 (2020) 1865–1874, <https://doi.org/10.1021/acsabm.9b00965>.
- [50] S. Tajbakhsh, F. Hajjiali, A comprehensive study on the fabrication and properties of biocomposites of poly(lactic acid)/ceramics for bone tissue engineering, *Mater. Sci. Eng. C* 70 (2017) 897–912, <https://doi.org/10.1016/j.msec.2016.09.008>.
- [51] T. Serra, J.A. Planell, M. Navarro, High-resolution PLA-based composite scaffolds via 3-D printing technology, *Acta Biomater.* 9 (2013) 5521–5530, <https://doi.org/10.1016/j.actbio.2012.10.041>.
- [52] T. Serra, M.A. Mateos-Timoneda, J.A. Planell, M. Navarro, 3D printed PLA-based scaffolds, *Organogenesis* 9 (2013) 239–244, <https://doi.org/10.4161/org.26048>.
- [53] R. Pecci, S. Baiguera, P. Ioppolo, R. Bedini, C. Del Gaudio, 3D printed scaffolds with random microarchitecture for bone tissue engineering applications: manufacturing and characterization, *J. Mech. Behav. Biomed. Mater.* 103 (2020), 103583, <https://doi.org/10.1016/j.jmbbm.2019.103583>.
- [54] H. Zhou, J.G. Lawrence, S.B. Badhuri, Fabrication aspects of PLA-CaP/PLGA-CaP composites for orthopedic applications: a review, *Acta Biomater.* 8 (2012) 1999–2016, <https://doi.org/10.1016/j.actbio.2012.01.031>.
- [55] L. Germain, C.A. Fuentes, A.W. van Vuure, A. des Rieux, C. Dupont-Gillain, 3D-printed biodegradable gyroid scaffolds for tissue engineering applications, *Mater. Des.* 151 (2018) 113–122, <https://doi.org/10.1016/j.matdes.2018.04.037>.
- [56] H. Liu, Y. Du, J.P. St-Pierre, M.S. Bergholt, H. Autefage, J. Wang, M. Cai, G. Yang, M.M. Stevens, S. Zhang, Bioenergetic-active materials enhance tissue regeneration by modulating cellular metabolic state, *Sci. Adv.* 6 (2020) 1–15, <https://doi.org/10.1126/sciadv.aay7608>.
- [57] E.C. Jensen, Quantitative analysis of histological staining and fluorescence using imageJ, *Anat. Rec.* 296 (2013) 378–381, <https://doi.org/10.1002/ar.22641>.
- [58] Y. Chen, Q. Yu, C.B. Xu, A convenient method for quantifying collagen fibers in atherosclerotic lesions by imagej software, *Int. J. Clin. Exp. Med.* 10 (2017) 14904–14910.
- [59] N.A. Iafe, N. Phasukkijwata, X. Chen, D. Sarraf, Retinal capillary density and foveal avascular zone area are age-dependent: quantitative analysis using optical coherence tomography angiography, *Investig. Ophthalmol. Vis. Sci.* 57 (2016) 5780–5787, <https://doi.org/10.1167/iovs.16-20045>.
- [60] C.C. Xu, R.W. Chan, Pore architecture of a bovine acellular vocal fold scaffold, *Tissue Eng. A* 14 (2008) 1893–1903, <https://doi.org/10.1089/ten.tea.2007.0243>.
- [61] S.T. Ho, D.W. Hutmacher, A comparison of micro CT with other techniques used in the characterization of scaffolds, *Biomaterials*. 27 (2006) 1362–1376, <https://doi.org/10.1016/j.biomaterials.2005.08.035>.
- [62] W. Gröllmann, S. Seidler, *Polymer Testing*, 2nd ed., Hanser Publications, 2013.
- [63] M. Ashby, H. Shercliff, D. Cebon, *Materials: Engineering, Science, Processing and Design*, 1st ed., Butterworth-Heinemann, 2007.
- [64] K.M. Fawzy El-Sayed, C.E. Dörfer, Gingival mesenchymal stem/progenitor cells: a unique tissue engineering gem, *Stem Cells Int.* 2016 (2016) 1–16, <https://doi.org/10.1155/2016/7154327>.
- [65] C. Millan, J.F. Vivanco, I.M. Benjumeda-Wijnhoven, S. Bjelica, J.F. Santibanez, Mesenchymal stem cells and calcium phosphate bioceramics: implications in periodontal bone regeneration, in: *Cell Biol. Transl. Med* vol. 3, Springer International Publishing, Cham, 2018, pp. 91–112.
- [66] I. Benjumeda Wijnhoven, R. Vallejos, J.F. Santibanez, C. Millán, J.F. Vivanco, Analysis of cell-biomaterial interaction through cellular bridge formation in the interface between hGMSCs and CaP bioceramics, *Sci. Rep.* 10 (2020), 16493, <https://doi.org/10.1038/s41598-020-73428-y>.
- [67] Z.T. Birgani, C.A. van Blitterswijk, P. Habibovic, Monolithic calcium phosphate/poly(lactic acid) composite versus calcium phosphate-coated poly(lactic acid) for support of osteogenic differentiation of human mesenchymal stromal cells, *J. Mater. Sci. Mater. Med.* 27 (2016) 1–12, <https://doi.org/10.1007/s10856-016-5669-9>.
- [68] C. Brown, C. McKee, S. Bakshi, K. Walker, E. Hakman, S. Halassy, D. Svinarich, R. Dodds, C.K. Govind, G.R. Chaudhry, *Mesenchymal stem cells: cell therapy and regeneration potential*, *J. Tissue Eng. Regen. Med.* 13 (2019) 1738–1755.
- [69] M. Schneider, N. Fritzsche, A. Pucil-Malinowska, A. Baliś, A. Mostafa, I. Bald, S. Zapotoczny, A. Taubert, Surface etching of 3D printed poly(lactic acid) with NaOH: a systematic approach, *Polymers (Basel)* 12 (2020), <https://doi.org/10.3390/POLYM12081711>.
- [70] I. Izal, P. Aranda, P. Sanz-Ramos, P. Ripalda, G. Mora, F. Granero-Moltó, H. Deplaine, J.L. Gómez-Ribelles, G.G. Ferrer, V. Acosta, I. Ochoa, J.M. García-Aznar, E.J. Andreu, M. Monleón-Pradas, M. Doblaré, F. Prósper, Culture of human bone marrow-derived mesenchymal stem cells on of poly(l-lactic acid) scaffolds: potential application for the tissue engineering of cartilage, *Knee Surg. Sports Traumatol. Arthrosc.* 21 (2013) 1737–1750, <https://doi.org/10.1007/s00167-012-2148-6>.
- [71] B.W. Chieng, N.A. Ibrahim, W.M.Z.W. Yunus, M.Z. Hussein, Poly(lactic acid)/poly(ethylene glycol) polymer nanocomposites: effects of graphene nanoplatelets, *Polymers (Basel)* 6 (2014) 93–104, <https://doi.org/10.3390/polym6010093>.
- [72] M.A. Pop, C. Croitoru, T. Bedő, V. Geaman, I. Radomir, M. Coșniță, S.M. Zaharia, L. A. Chicoş, I. Miloşan, Structural changes during 3D printing of bioderived and synthetic thermoplastic materials, *J. Appl. Polym. Sci.* 136 (2019) 1–11, <https://doi.org/10.1002/app.47382>.
- [73] Y. Song, Y. Li, W. Song, K. Yee, K.-Y. Lee, V.L. Tagarielli, Measurements of the mechanical response of unidirectional 3D-printed PLA, *Mater. Des.* 123 (2017) 154–164, <https://doi.org/10.1016/j.matdes.2017.03.051>.
- [74] D. Kazmer, in: M.B.T.-A.P.E.H (Ed.), *28 - Three-Dimensional Printing of Plastics*, Second E. Kutz, Plast. Des. Libr., William Andrew Publishing, 2017, pp. 617–634, <https://doi.org/10.1016/B978-0-323-39040-8.000029-8>.
- [75] L. Galois, D. Mainard, Bone ingrowth into two porous ceramics with different pore sizes: an experimental study, *Acta Orthop. Belg.* 70 (2004) 598–603.
- [76] R.M. Schek, E.N. Wilke, S.J. Hollister, P.H. Krebsbach, Combined use of designed scaffolds and adenoviral gene therapy for skeletal tissue engineering, *Biomaterials*. 27 (2006) 1160–1166, <https://doi.org/10.1016/j.biomaterials.2005.07.029>.
- [77] S.J. Hollister, C.Y. Lin, E. Saito, C.Y. Lin, R.D. Schek, J.M. Taboas, J.M. Williams, B. Partee, C.L. Flanagan, A. Diggs, E.N. Wilke, G.H. Van Lenthe, R. M??ller, T. Wirtz, S. Das, S.E. Feinberg, P.H. Krebsbach, Engineering craniofacial scaffolds, *Orthod. Craniofacial Res.* 8 (2005) 162–173, <https://doi.org/10.1111/j.1601-6343.2005.00329.x>.
- [78] J.A. Choren, S.M. Heinrich, M.B. Silver-Thorn, Young's modulus and volume porosity relationships for additive manufacturing applications, *J. Mater. Sci.* 48 (2013) 5103–5112, <https://doi.org/10.1007/s10853-013-7237-5>.
- [79] Z. Hashin, The elastic moduli of heterogeneous materials, *J. Appl. Mech.* 29 (1962) 143–150, <https://doi.org/10.1115/1.3636446>.
- [80] D.P.H. Hasselman, On the porosity dependence of the elastic moduli of polycrystalline refractory materials, *J. Am. Ceram. Soc.* 45 (1962) 452–453, <https://doi.org/10.1111/j.1151-2916.1962.tb11191.x>.
- [81] C.T. Herakovich, S.C. Baxter, Influence of pore geometry on the effective response of porous media, *J. Mater. Sci.* 34 (1999) 1595–1609, <https://doi.org/10.1023/A:1004528600213>.
- [82] A.K. Maitra, K.K. Phani, Ultrasonic evaluation of elastic parameters of sintered powder compacts, *J. Mater. Sci.* 29 (1994) 4415–4419, <https://doi.org/10.1007/BF00376263>.
- [83] R.W. Rice, Evaluation and extension of physical property-porosity models based on minimum solid area, *J. Mater. Sci.* 31 (1996) 102–118, <https://doi.org/10.1007/BF00355133>.
- [84] A.P. Roberts, E.J. Garboczi, Elastic properties of porous ceramics, *J. Am. Ceram. Soc.* 83 (2000) 3041–3048, <https://doi.org/10.1111/j.1151-2916.1961.tb11671.x>.
- [85] R.M. Spriggs, Expression for effect of porosity on elastic modulus of polycrystalline refractory materials, particularly aluminum oxide, *J. Am. Ceram. Soc.* 44 (1961) 628–629, <https://doi.org/10.1111/j.1151-2916.1961.tb11671.x>.
- [86] L.R. Jaidev, K. Chatterjee, Surface functionalization of 3D printed polymer scaffolds to augment stem cell response, *Mater. Des.* 161 (2019) 44–54, <https://doi.org/10.1016/j.matdes.2018.11.018>.
- [87] S. Noh, N. Myung, M. Park, S. Kim, S.-U. Zhang, H.-W. Kang, 3D bioprinting for tissue engineering, in: B.W. Kim (Ed.), *Clin. Regen. Med. Urol.*, Springer, Singapore, Singapore, 2018, pp. 105–123, https://doi.org/10.1007/978-981-10-2723-9_5.
- [88] M.-H. Ho, P.-Y. Kuo, H.-J. Hsieh, T.-Y. Hsien, L.-T. Hou, J.-Y. Lai, D.-M. Wang, Preparation of porous scaffolds by using freeze-extraction and freeze-gelation methods, *Biomaterials*. 25 (2004) 129–138, [https://doi.org/10.1016/S0142-9612\(03\)00483-6](https://doi.org/10.1016/S0142-9612(03)00483-6).
- [89] C.N. Kelly, A.T. Miller, S.J. Hollister, R.E. Guldberg, K. Gall, Design and structure-function characterization of 3D printed synthetic porous biomaterials for tissue engineering, *Adv. Healthc. Mater.* 7 (2018) 1–16, <https://doi.org/10.1002/adhm.201701095>.
- [90] A. Grémare, V. Guduric, R. Bareille, V. Heroguez, S. Latour, N. L'heureux, J. C. Fricain, S. Catros, D. Le Nihouannen, Characterization of printed PLA scaffolds for bone tissue engineering, *J. Biomed. Mater. Res. A* 106 (2018) 887–894, <https://doi.org/10.1002/jbm.a.36289>.
- [91] A. Souness, F. Zamboni, G.M. Walker, M.N. Collins, Influence of scaffold design on 3D printed cell constructs, *J. Biomed. Mater. Res. B Appl. Biomater.* 106 (2017) 533–545, <https://doi.org/10.1002/jbm.b.33863>.